Applied Surface Science Advances 19 (2024) 100569

Contents lists available at ScienceDirect

Applied Surface Science Advances

journal homepage: www.sciencedirect.com/journal/applied-surface-science-advances

Spent Li-ion batteries derived synthesis of boron doped RGO-Bi_2WO_6 for photocatalytic degradation of antibiotics

K. Yogesh Kumar [a], M.K. Prashanth [b], H. Shanavaz [a], L. Parashuram [c], Fahd Alharethy [d], Byong-Hun Jeon [e,*], V.S. Anusuya Devi [f], M.S. Raghu [f,*]

[a] Department of Chemistry, Faculty of Engineering and Technology, Jain University, Bangalore 562112, India
[b] Department of Chemistry, BNM Institute of Technology, Banashankari, Bangalore 560070, India
[c] Department of Chemistry, Nitte Meenakshi Institute of Technology, Yelahanka, Bangalore 560064 India
[d] Department of Chemistry, College of Science, King Saud University, Riyadh 11451, Saudi Arabia
[e] Department of Earth Resources and Environmental Engineering, Hanyang University, 222, Wangsimni-ro, Seongdong-gu, Seoul 04763, Republic of Korea
[f] Department of Chemistry, New Horizon College of Engineering, Outer Ring Road, Bangalore 560103, India

ARTICLE INFO

Keywords:
E-waste derived BRGO
Li-ion battery recycle
Bi_2WO_6
Pharmaceuticals
Photocatalysis

ABSTRACT

The aim of the current study is to resolve two significant environmental cleanup issues. The first involves recycling the spent lithium-ion batteries (LIBs) and the second involves the degradation of the antibiotics found in water. It has been possible to synthesize reduced graphene oxide (RGO) from used LIBs that have also been doped with boron (BRGO). A nanocomposite (BWO/BR) is formed when BRGO and a visible active Bi_2WO_6 (BWO) are mixed together. The structural, morphological, and spectroscopic characterizations confirm the formation of BRGO, BWO, and BWO/BR nanocomposite. The antibiotics tetracycline hydrochloride (TCH) and ciprofloxacin (CIP) have been tested for photocatalytic degradation with all three of the newly made materials. It is found to decrease the bandgap of BWO (2.73 eV) to 2.22 eV upon combining with BRGO. Under visible light, BWO/BR exhibits elevated TCH degradation (93 %), which is found to increase in the presence of sunlight (95 %). In the presence of BWO/BR, the degradation of CIP was reported to be 72, 95, and 97.5 % in UV, visible, and sunlight, respectively. The effect of reaction conditions like pH, amount of catalyst and initial concentration were examined towards degradation of TCH and CIP in presence of BWO/BR. It has been discovered that pH 6 and 8 are ideal for TCH and CIP, respectively. Studies on TCH and CIP degradation in pharmaceutical effluent were also conducted; in the presence of BWO/BR and visible light, the degradation efficiencies were determined to be 69 and 72 %, respectively. All of the zone of inhibition of *E. Coli,* L. *monocytogenes, S. typhimurium,* and *S. aureus* were examined in presence of BWO/BR before and after exposure to visible light for 90 min, during which time a near-zero zone of inhibition was seen. There were investigations using liquid chromatography-mass spectrometry (LC-MS) to identify the intermediate products of TCH and CIP degradation.

1. Introduction

The presence of antibiotics in our environment, especially in water sources, has become a major worldwide concern with far-reaching effects [1,2]. In earlier decades, antibiotics were hailed as life-saving wonders of modern medicine and are now posing a hazardous threat due to their extensive accumulation in aquatic ecosystems [3,4]. Antibiotics are widely used in both human and veterinary medicine, and they are also used in agricultural practices, which has led to this worrying trend. Due to less awareness about toxicity, improper disposal to rivers, lakes, and oceans is observed [5]. These powerful medications represent a serious risk to human health as well as upsetting delicate ecological balances [6]. Therefore, addressing this global environmental health crisis is in high demand, which targets post-disposal treatment of antibiotics in an aqueous system [7,8].

Tetracycline hydrochloride ((4S,6S,12aS)−4-(dimethylamino)−1,4,4a,5,5a,6,11,12a-octahydro-3,6,10,12,12a-pentahydroxy-6-methyl-1,11-dioxonaphthacene-2-carboxamide) and ciprofloxacin (1-cyclopropyl-6-fluoro-4-oxo-7-piperazin-1-ylquinoline-3-carboxylic acid) are the two extensively produced and used pharmaceuticals due to high antimicrobial activity and low cost. The improper metabolism, unused and expired antibiotics released by pharmaceutical industries, and

* Corresponding authors.
E-mail addresses: bhjeon@hanyang.ac.kr (B.-H. Jeon), dr.msraghu@newhorizonindia.edu (M.S. Raghu).

https://doi.org/10.1016/j.apsadv.2023.100569
Received 30 September 2023; Received in revised form 19 December 2023; Accepted 28 December 2023
Available online 3 January 2024

sewage sludge cause environmental issues [9,10]. The amount of TCH and CIP accumulation has grown from nano- to micro-level. Among the several methods available for the treatment of pollutants, photocatalysis stands out first due to the complete mineralization of the organic molecules into carbon dioxide and water [11–15]. Compared to the Advanced Oxidation Process (AOP) and sonophotocatalysis, direct photocatalysis in the presence of semiconductors that harness visible light is proven to be a simple, effective, environmentally benign, and cost-effective method for the degradation of TCH and CIP [16–18].

Bi_2WO_6 (BWO) is an n-type semiconductor with a band gap of ~ 2.8 eV formed by a perovskite-like slab of $(Bi_2O_2)^{+2}$ and $[WO_4]^{2-}$ [19–21]. The orthorhombic crystalline state of BWO, with its non-toxicity, stability, and efficient capability to utilize visible light, finds applications in NO and CO_2 reduction, H_2 evolution, organic molecule degradation, supercapacitors, and other energy storage applications [22–28]. However, its visible light response range is limited (420–460 nm), and its photogenerated electron-hole pair recombination rate is significant, limiting its usefulness. Hence, BWO is preferred to combine with other noble metals, metal oxides, or carbon-based materials to boost its photocatalytic activity even more [29–31,29].

Graphene-based materials have gained high importance due to their flexibility, strength, conductivity, and surface area and find various applications in energy harnessing and storage [32–34]. Reduced graphene oxide (RGO), which is generated from graphene oxide via a reduction process, has more photocatalytic potential than virgin graphene. During the reduction process, the introduction of defects and oxygen-containing functional groups increases its reactivity and produces active sites for photocatalytic processes [35]. Nonetheless, RGO's bandgap limits its response to visible light. Boron doping in RGO is the incorporation of boron atoms into the RGO carbon lattice. Even at a large activation energy barrier of 2.6–2.8 eV, boron (B) can replace carbon (C) due to its nearby covalent atomic radii (85 pm for B and 70 pm for C). This intentional alteration endows the material with numerous important photocatalytic properties [36,37]. Adding boron to RGO changes its absorbance towards the visible range. This creates areas in RGO that do not have enough electrons, which leads to the creation of more active sites and better photocatalysis [38,39].

Scotch tape, chemical vapor deposition, epitaxial growth, CNT unzipping, and other methods have been devised for the synthesis of GO [40,41]. All of the methods make use of pure graphite, which is expensive and scarce everywhere except in India and China. Lithium-ion batteries (LIBs) are extensively used in portable gadgets, mobile phones, electric vehicles, cameras, and laptops. Spent LIBs typically consist of an anode, cathode, electrolyte, and separator—the polymer. The cathode is made up of lithium metal oxide, while the anode is made up of graphite [42]. After their useful lives are up, a large proportion of LIBs are thrown into the ecosystem as electronic waste, which severely harms the environment by polluting the land, atmosphere, and water systems [43]. Furthermore, metals and organic electrolytes will cause serious health issues for people. Therefore, in order to protect our environment, it is crucial to recycle spent LIBs in an appropriate and effective manner. The production of graphene oxide from spent LIBs is an exciting and environmentally sustainable method of recycling LIB materials while also providing a valuable carbon-based material with multiple applications [44]. Because of their high energy density and long cycle life, LIBs have become common power sources in modern devices and electric vehicles. [45]. An innovative and environmentally friendly method that could have a significant influence is the synthesis of boron-doped reduced graphene oxide BWO/BR from used Li-ion batteries for the photocatalytic degradation of antibiotics. An eco-friendly and sustainable method for carbon source from Li-ion batteries as a source for raw materials. This improves recycling efforts while simultaneously dealing with the problem of electronic trash. The utilization of recyclable resources and the environmentally friendly synthesis process make this technology more attractive for use in industrial settings. This improves recycling efforts while simultaneously dealing with the problem of electronic trash Synthesizing RGO from LIBs exhibits several advantages compared to many available methods; LIBs are the readily available source of carbon-rich materials, reduce the mining of graphite, reduce electronic waste, and thereby reduce the environmental impact. They are also cost-effective and reduce carbon footprint during mining, which promotes resource conservation, waste reduction, and circular economy principles while providing a valuable substance with numerous applications [46,47]. Using recycled resources, minimizing waste, and applying eco-friendly synthesis methods, the process as a whole may be in line with green chemistry principles. Ultimately, the novelty of this work lies in its development of a photocatalyst for antibiotic degradation that combines boron doping, RGO as a support material, and recycled Li-ion batteries. This method tackles sustainability and environmental issues while also making a contribution to materials science.

The current work focuses on mainly on environmental remediation in two ways. Initially, carbon for the synthesis of BRGO is obtained from spent Li-ion batteries. The other is boosting the photocatalytic breakdown of antibiotics by employing the synthesized BRGO as a supporting material. B-doped RGO is combined with BWO to generate BWO/BR nanocomposite. Evaluations have been conducted on structural, morphological, and photo/electrochemical characterizations. A good degradation efficiency was achieved even in simultaneous degradation of TCH and CIP. Pharmaceutical wastewater is also subjected to degradation experiments, which reveal the degradation of 72 and 69 % of TCH and CIP, respectively. The current work will serve as a guide for future investigations into the recycling of LIBs and their efficient application in water treatment.

2. Experimental

2.1. Materials

Bismuth (III) nitrate pentahydrate (Bi $(NO_3)_3{\cdot}5H_2O$), sodium tungstate dehydrate ($Na_2WO_4{\cdot}2H_2O$), boric acid (H_3BO_3), sodium chloride (NaCl), sodium hydroxide (NaOH), hydrochloric acid (HCl) Ethylenediaminetetraacetic acid (EDTA), benzoquinone, Tertiary butyl alcohol and ethanol were procured from Fisher Scientific India Pvt. Ltd. in Mumbai, India. All chemicals (Analytical grade reagents, AR) were used in the experiments, without further purifications. 99.99 % TCH and CIP samples were received as gift from Advinus Therapeutics Ltd. Bangalore, India.

2.2. Synthesis of BRGO, BWO and BWO/BR

In continuation to our previous work wherein we have synthesized RGO from the primary batteries [40]. In the present study, spent or dead lithium-ion batteries are collected from the SP road market in Bangalore, India. Before subjecting to experimental conditions, all the batteries were dipped in saturated solution of NaCl for the complete discharge of the batteries. This process will avoid the fire or explosion during recycling process. Both physical and chemical methods were employed to separate anode, cathode, separator and electrolyte from the batteries. Initially, the outer layer usually made up of stainless steel were dismantled and separated the anode and cathode. Usually, anode material in which graphite is deposited on the surface of copper foil were separated by immersing the anode material in the aqueous solution stirred for 2 h under ultrasonication. The graphite powders were collected and heated to 600 °C for 6 h to remove all other impurities.

Graphite powder obtained in the above step was used as the feed for the synthesis of BRGO. Modified hummers method was used for the synthesis of graphene oxide as explained in our previous work [40]. 100 mg of GO and 500 mg of boric acid was transferred in to a beaker with 25 mL of distilled water. Solution was stirred continuously for 4 h at room temperature. Then the solution was transferred in to autoclave for hydrothermal treatment for 6 h at 140 °C. As purification step the sample obtained is stirred for 30 min with 1 M NaOH to remove

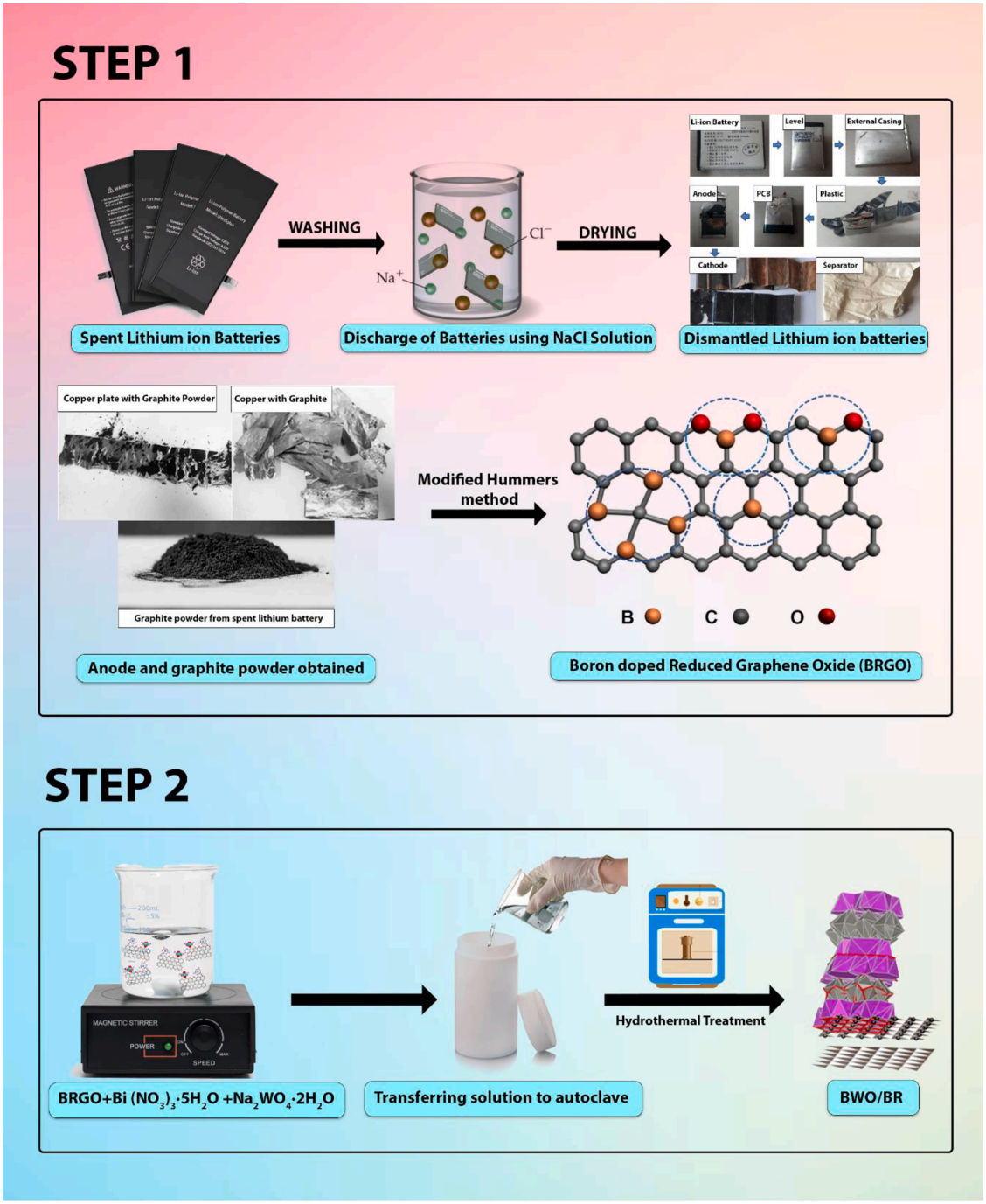

Scheme 1. Synthetic scheme of BRGO and BWO/BR.

unreacted boric acid. Then the sample was washed with water, alcohol for three time and dried in an oven at 60 °C for overnight.

50 mg of BRGO was dispersed in a 100 mL of water and stirred continuously. Equimolar proportion of Bi $(NO_3)_3{\cdot}5H_2O$ and $Na_2WO_4{\cdot}2H_2O$ added to the same solution drop wise before that 5 mL of Triton X 100 was used which act as surfactant. The entire mixture has been transferred in to 100 mL stainless steel hydrothermal bomb lined inside with Teflon coated autoclave and heated at 180 °C for 6 h. the autoclave has been allowed to cool naturally then the precipitate obtained was washed continuously with water and alcohol and dried in an oven to collect the BRGO. BWO has been synthesized by using the same method without adding BRGO for the purpose of comparison studies. The entire synthetic procedure is depicted in Scheme 1.

2.3. Photocatalytic degradation of TCH and CIP

BWO, BRGO and BWO/BR were examined for photocatalytic degradation of TCH and CIP. A stock solution of 100 mg L^{-1} of TCH and CIP was prepared and kept in the dark when not in use. In a 250-mL quartz vessel, 200 mL of 10 mg L^{-1} TCH and CIP solutions were taken for degradation studies. A mercury vapor lamp of 250 W (OSRAM HQL 250, 12,200 lm) and a Xe lamp of 300 W (MARUTEK, 7090 lm) were used as UV and visible light sources, respectively. The UV and visible light source lamps were placed at placed at a distance of 15 cm from the flask .The degradation studies were also carried out under solar radiation during the summer (March and April, having the flux 25,245 to 30,867 lm) in Bangalore, India, between 11.30 am and 3.30 pm. 20 mg

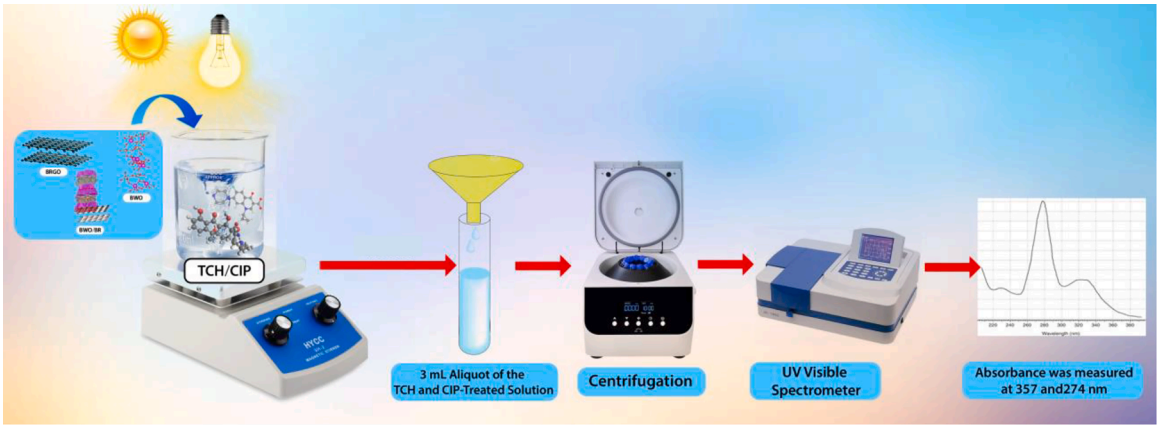

Scheme 2. Schematic representation of photocatalytic degradation studies of TCH and CIP.

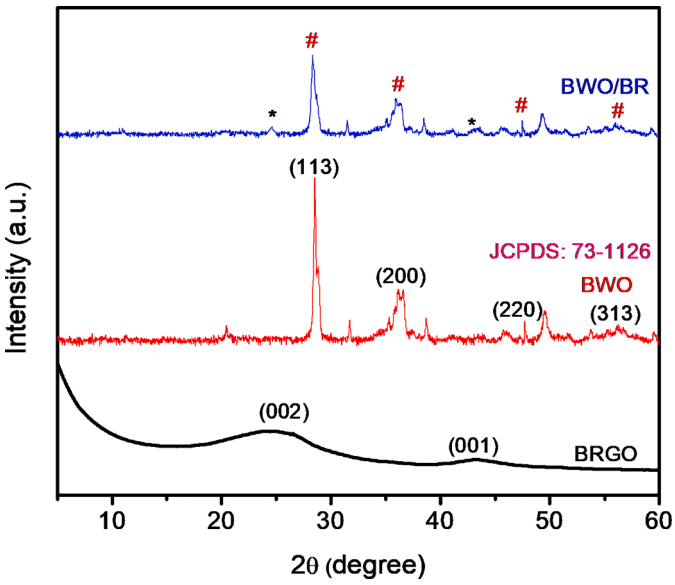

Fig. 1. XRD of BRGO, BWO and BWO/BR.

(for TCH) and 30 mg (CIP) of BWO/BR were added; the pH was set to 6 and 8 for the TCH and CIP solutions, respectively; and the solution was dispersed using an ultrasonicator before being stirred continuously with a magnetic stirrer. After the attainment of adsorption/desorption equilibrium (30 min), a 3 mL aliquot of the TCH and CIP-treated solution was centrifuged at 1200 rpm, and absorbance was measured at 357 and 274 nm, respectively, using a UV–visible spectrophotometer (Shimadzu UV-1600) as shown in Scheme 2. The photocatalytic degradation percentage was evaluated using Eq. (1).

$$\%\ degradation = \frac{C_o - C}{C_o} \times 100 \quad (1)$$

Where, C_o is initial and C is final concentrations of TCH and CIP.

2.4. Characterization

To comprehend the structural properties of the synthesized materials, X-ray diffraction experiments were carried out utilizing Bruker D2 Phaser XRD equipment with Cu-Kα radiation. With a 5 kV acceleration voltage, a JEOL JSM 840A energy-dispersive X-ray spectrometer (EDS) was used to record images from SEM and FESEM. TEM pictures were captured in JEOL/JEM 2100 with a 200 kV acceleration voltage. The degradation studies of pharmaceutical solutions and the absorbance of prepared samples (UV-DRS) were recorded using the Shimadzu UV-1600 model. The photoluminescence investigation was carried out in the RF-6000 spectroflurometer. For TOC removal investigations, a fusion UV/persulfate Total Organic Carbon (TOC) analyzer (Teledyne Tekmar, USA) was utilized. Using a CHI 660 D electrochemical workstation, the photoelectrochemical characterization of the synthesized materials was assessed. Ag/AgCl and Pt wire serve as the reference and counter electrodes, respectively, in the unit's three-electrode setup. 15 mg of the material were used to create a functioning electrode, which was then sonicated in a 0.5 % Nafion solution. 20 μL of the suspension was dropcast, dried and used for Mott-Schottky, photocurrent, and electrochemical impedance investigations.

3. Results and discussion

3.1. Structural and morphological characterization

Fig. 1 shows the diffractogram of BRGO, BWO, and BWO/BR nanocomposite. The peaks found in the 2θ 24.5° and a small peak in the range

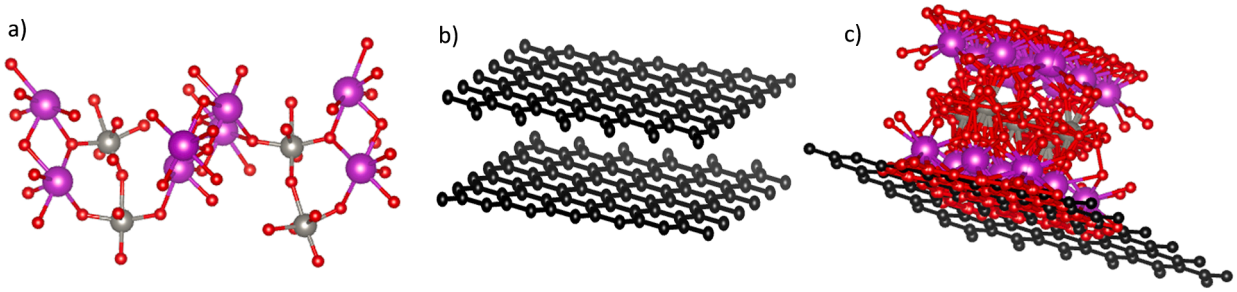

Fig. 2. Simulated crystalline structures of (a) BRGO, (b) BWO and (c) BWO/BR.

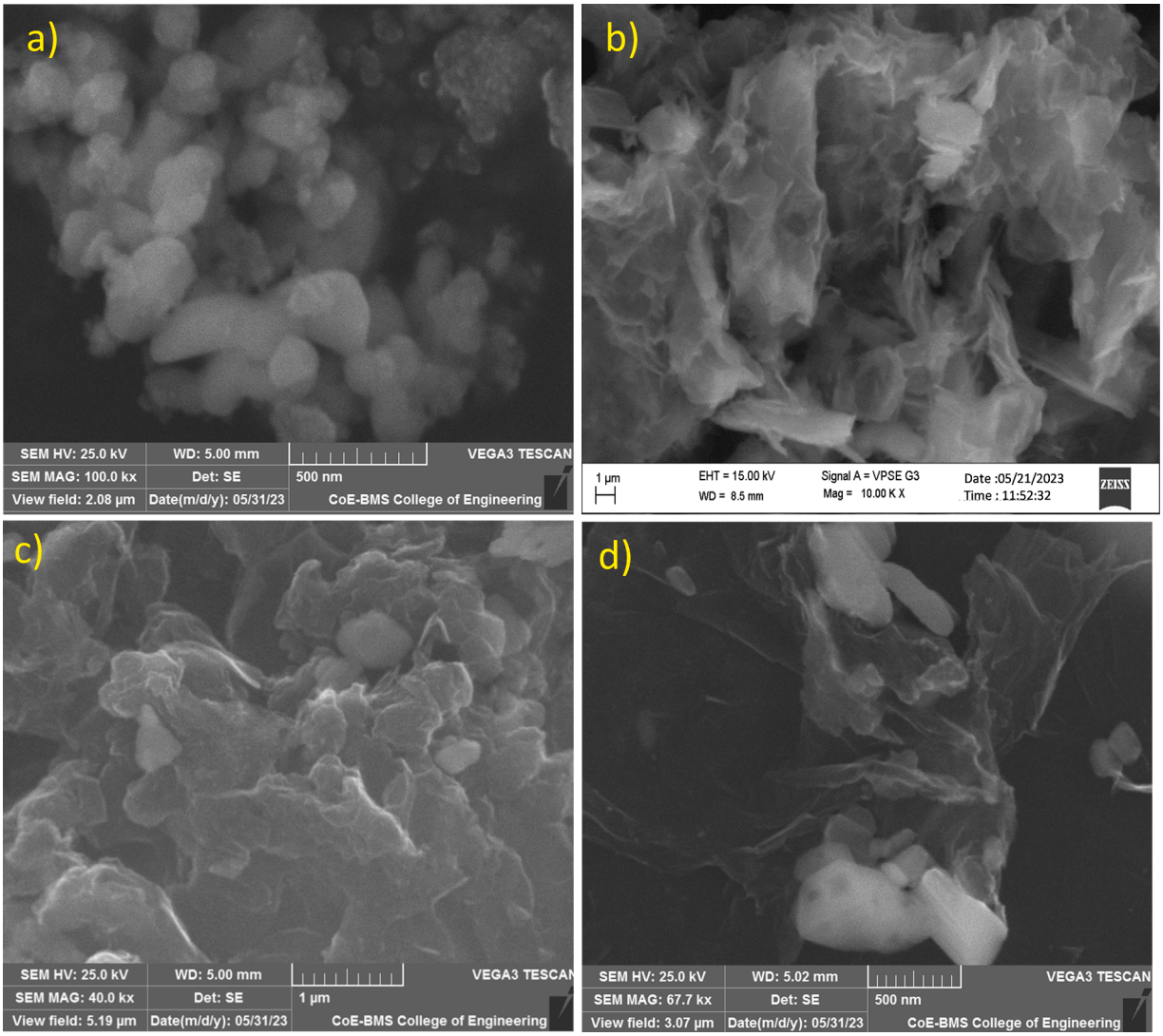

Fig. 3. SEM monographs of (a) BWO, (b) BRGO, (c&d) BWO/BR.

of 42.9° are corresponds to the (002) and (100) plane of BRGO respectively. The XRD peaks of pristine BRGO was found to be broad and even after boron doping the sample has retained its hexagonal structure and this broadening is also indicates the defects induced upon doping of boron. For BWO the diffractogram clearly shows the formation of orthorhombic structure indexed to the JCPDS card no 73-1126 [48]. The peaks at 28.5, 36.5, 47.7, and 56.06°, corresponding to (113), (200), (220) and (313) crystal planes respectively. BWO/BR composites retained the peaks of both BRGO and BWO at the same time full widths at half maximum (FWHM) of the composites slightly larger than the ones of non-doped BWO, indicating a crystallization poorer than the crystallization of non-doped BWO, implying an improvement in the formation of nanosized particles. X-Ray diffraction peaks of the composite material is very similar to that of the pure BWO. Note that the absence of a graphitic carbon peak corresponding to BRGO is due to its low intensity relative to the peaks of BWO contained in the composite. Moreover, there is a possibility of much reduced restacking of the BRGO sheets in the composite material.

To get in to further insight of the crystal structure of the materials, polyhedron representation of BWO was studied using VESTA program. Fig. 2a shows that BWO crystallizes in the orthorhombic $Pca2_1$ space group. W^{6+} is bonded to six O^{2-} atoms to form distorted corner-sharing WO_6 octahedra. The corner-sharing octahedral tilt angles range from 20 to 29°. There are a spread of W–O bond distances ranging from 1.81 to 2.16 Å. There are two inequivalent Bi^{3+} sites. In the first Bi^{3+} site, Bi^{3+} is bonded in a 6-coordinate geometry to six O^{2-} atoms. There are a spread of Bi–O bond distances ranging from 2.20 to 2.52 Å. In the second Bi^{3+} site, Bi^{3+} is bonded in a 7-coordinate geometry to seven O^{2-} atoms. There are a spread of Bi–O bond distances ranging from 2.20 to 2.99 Å. There are six inequivalent O^{2-} sites. In the first O^{2-} site, O^{2-} is bonded to four equivalent Bi^{3+} atoms to form a mixture of distorted corner and edge-sharing Obi_4 tetrahedra. In the second O^{2-} site, O^{2-} is bonded in a 3-coordinate geometry to one W^{6+} and two equivalent Bi^{3+} atoms. In the third O^{2-} site, O^{2-} is bonded in a distorted bent 150° geometry to two equivalent W^{6+} and one Bi^{3+} atom. In the fourth O^{2-} site, O^{2-} is bonded in a distorted bent 150° geometry to two equivalent W^{6+} atoms. In the fifth O^{2-} site, O^{2-} is bonded in a 3-coordinate geometry to one W^{6+} and two equivalent Bi^{3+} atoms. In the sixth O^{2-} site, O^{2-} is bonded to four equivalents Bi^{3+} atoms to form a mixture of distorted corner and edge-sharing Obi_4 tetrahedra. Fig. 2b depicts the layered structure of BRGO. Similarly possible crystal structure of BWO/BR has been depicted in Fig. 2c which clearly shows that BWO can be firmly affixed on the BRGO sheet like structure which is in accordance with the XRD and SEM results.

Morphological characterization of the materials were explored by using SEM and TEM studies. Fig. 3 shows the SEM images of the BWO, BRGO and BWO/BR composites. Fig. 3a shows the SEM micrograph of BWO which consist more or less spherical particles with the slight

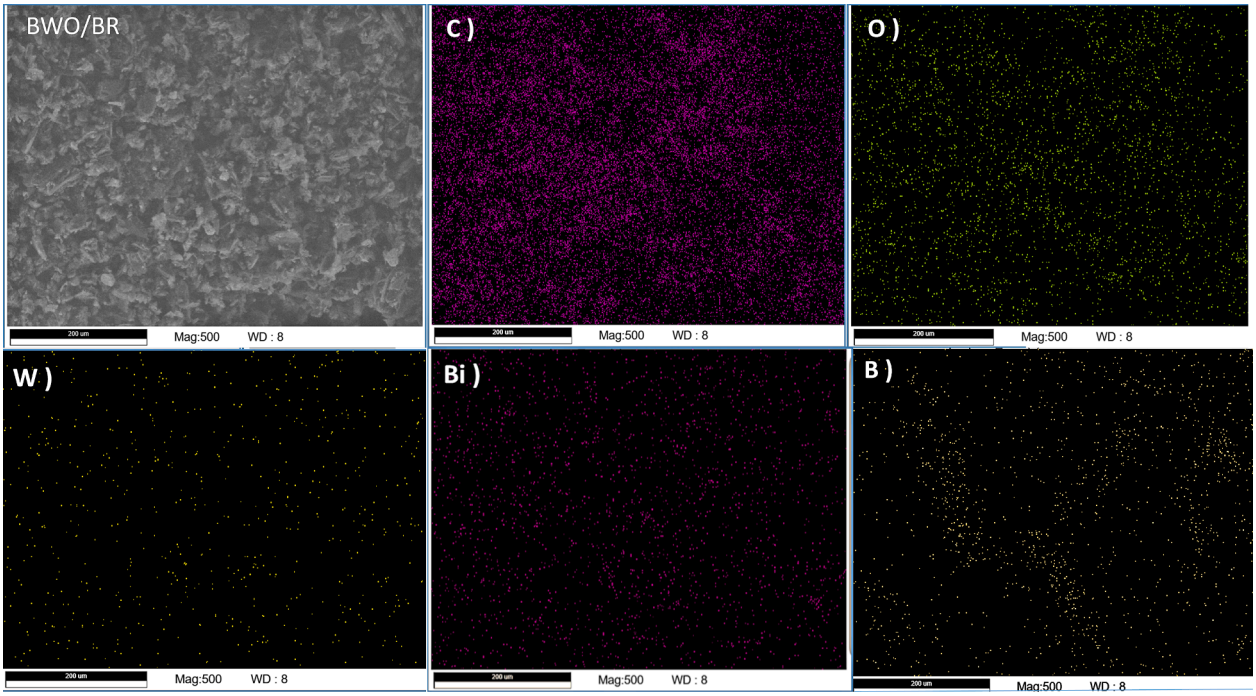

Fig. 4. EDS mapping of BWO/BR.

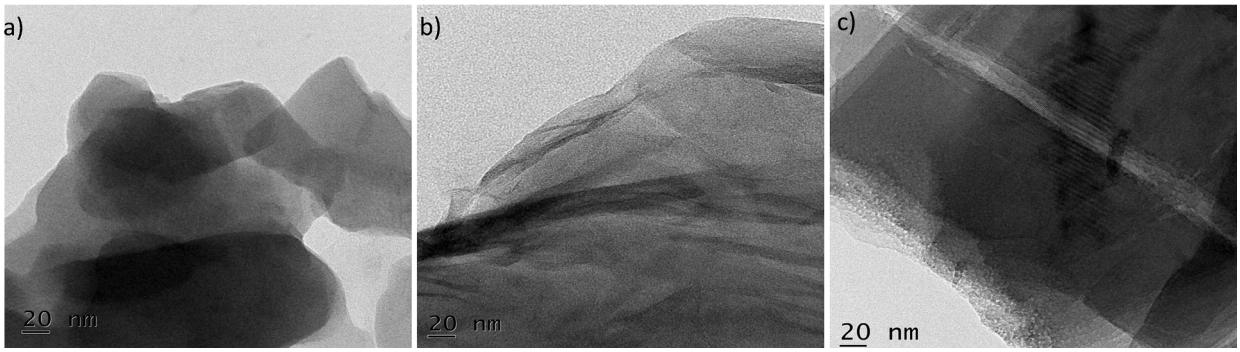

Fig. 5. TEM monographs of (a) BWO, (b) BRGO and (c) BWO/BR.

aggregation. BRGO clearly shows the formation of two-dimensional, wrinkled sheet like structure due to restacking of the layered structure (Fig. 3b). This sheet like structures is very closely packed in an two dimension layer in BRGO is due to the fact that oxygen functional groups are partially removed and the introduction of boron on the sheet like structure. The SEM images of BWO/BR (Fig. 3c&d) display the formation sheet like structure of BRGO surrounding the spherical BWO particles with large surface area this type formation may be due to the hydrothermal treatment. Thereby the active sites of this composite materials increase and thus increases the electron mobility. If we notice in the composite material morphology of the BWO also not been changed drastically might be due to the adherence of the particles on the BRGO surface then supporting the growth of the crystal which could promote the nanosheets self-assembly and the rate of the nucleation and precipitation..

EDS spectrum (Fig. 4) was used to understand the composition of the material which indicates the presence of B, C, Bi, W, and O without any further impurities. The monographs shows the uniform distribution of the elements throughout which certainly improves the catalytic efficiency in presence of light.

Further confirmation of the morphology was done using TEM studies, in which BWO particles confirms the presence of well separated particles with small aggregation (Fig. 5a). Fig. 5b show the wavy silk veil morphology of BRGO and these transparent sheets are entangled with one another. As evidence from the Fig. 5c that, BWO particles are covered with the BRGO sheets due to the electrostatic self-assembly. Separation of the photogenerated charge carriers is aided by the homogenous attachment of BWO on the BRGO sheets and the intimate interfacial contact between the two electron transporters.

The XPS method was used to analyze the samples for further details about the chemical composition, purity, and surface valence state and also to explore electronic interaction between BWO and BRGO. The survey spectrum (Fig. 6a) prominently display the presence of C, Bi, W, O and B. Fig. 6b depicts the high resolution XPS of Bi 4f; Bi^{+3} valence state is supported by the appearance of a Bi 4f doublet with binding energy values of 164.8 eV for Bi $4f_{5/2}$ and 159.3 eV for Bi $4f_{7/2}$ [49]. The broadness of the Bi 4f peaks suggests that the valence state of Bi in some of the nanosheets is +3 [50]. It was evidence that oxygen vacancies were present. Fig. 6c shows the XPS of W 4f composed of two peaks at 37.1 and 35.1 eV attributed to W $4f_{5/2}$ and W $4f_{7/2}$, respectively. We can infer +6 valence states with oxygen vacancies from the W peak value. The peaks of Bi 4f and W 4f show the deviation in their peak positions compared to pure BWO (Fig. S1). The deviation towards higher binding energy indicates the formation of composite with BRGO. Oxygen was

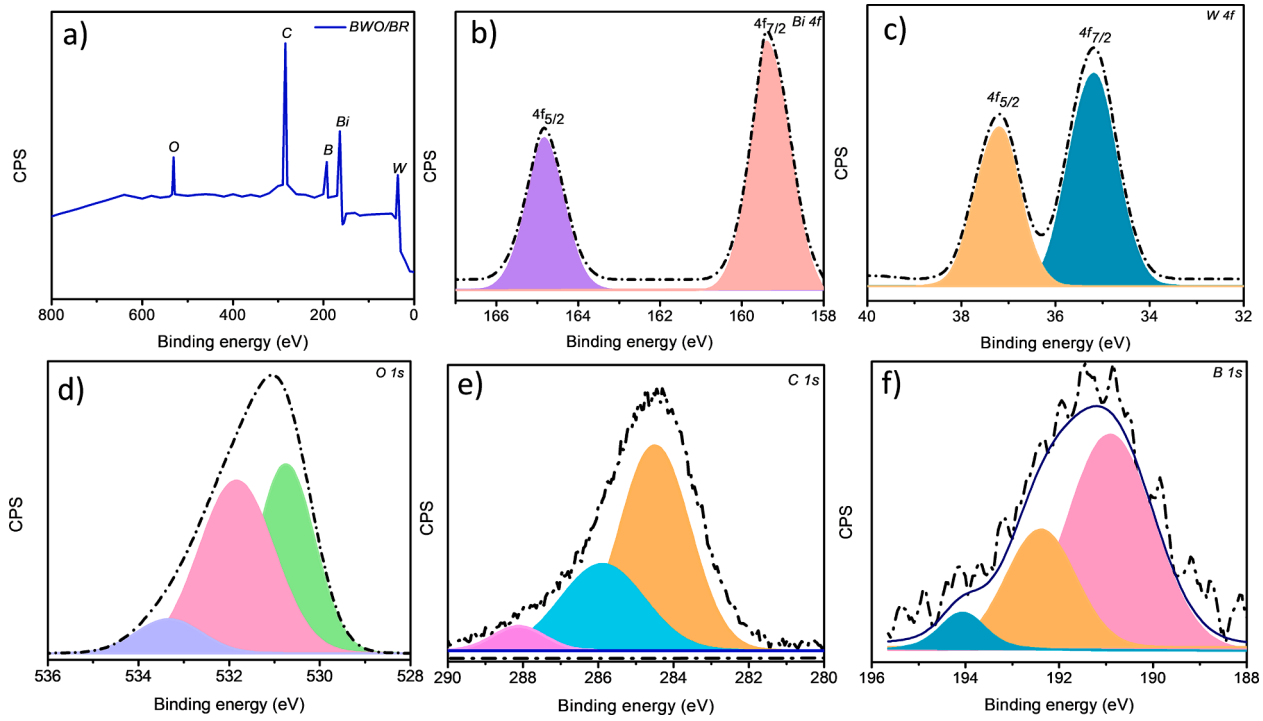

Fig. 6. XPS of BWO/BR (a) Survey spectrum (b) Bi 4f, (c) W 4f, (d) O 1s, (e) C 1s and (f) B 1s.

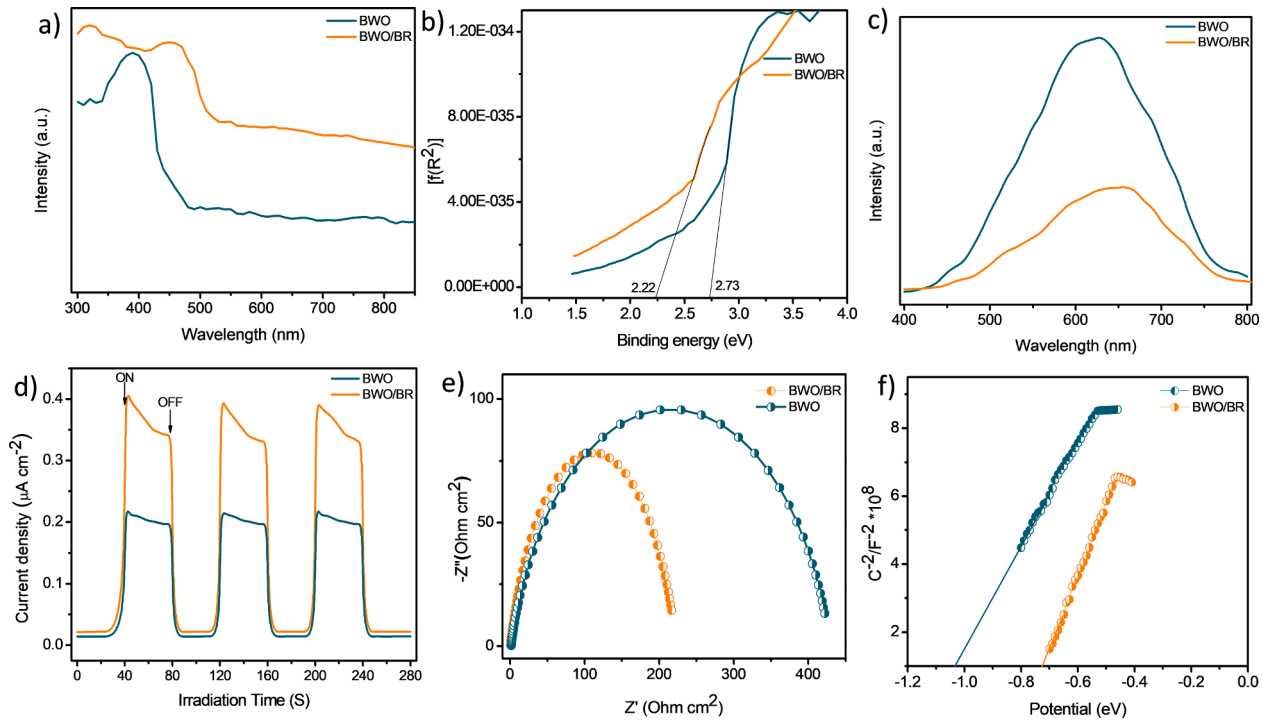

Fig. 7. (a) UV–Vis spectra of BWO and BWO/BR, (b)Kubelka-Munk curves of BWO and BWO/BR, (c) Photoluminescence spectra of BWO and BWO/BR, (d) Transient Photocurrent response of BWO and BWO/BR, (e) EIS curves of BWO and BWO/BR, and (f) Mott–Schottky plots BWO and BWO/BR.

shown to have a significant impact on the resolution scan of W and Bi. O1s scan is asymmetric and skewed to the higher binding energy (BE) side, showing an appearance at 533.8 eV (Fig. 6d). Type I bonding occurs when O has the lowest BE (530.7 eV) due to its metal bonding, type II bonding occurs when O has a high BE (533.38 eV) due to loosely bonded oxygen at the surface of the catalyst, and type III bonding occurs when O has a BE of roughly 531.8 eV. The oxygen-Bi-and-W-bonding process is responsible for the observed peak at 530.7 eV. Oxygen's rising BE reflected a corresponding drop in the lattice's valence electron density. As the BE of O 1s rises, the metal-oxygen bonds weaken, allowing for greater oxygen mobility in the lattice with vacancies in the composite. Three distinct peaks can be identified from the C1s spectra of (Fig. 6e) belongs to sp^2-hybridized carbon (C-C), epoxy/alkoxy carbon (C=O), and carboxylic carbon (O=C=O) at BE 284.45, 285.85, 288.18

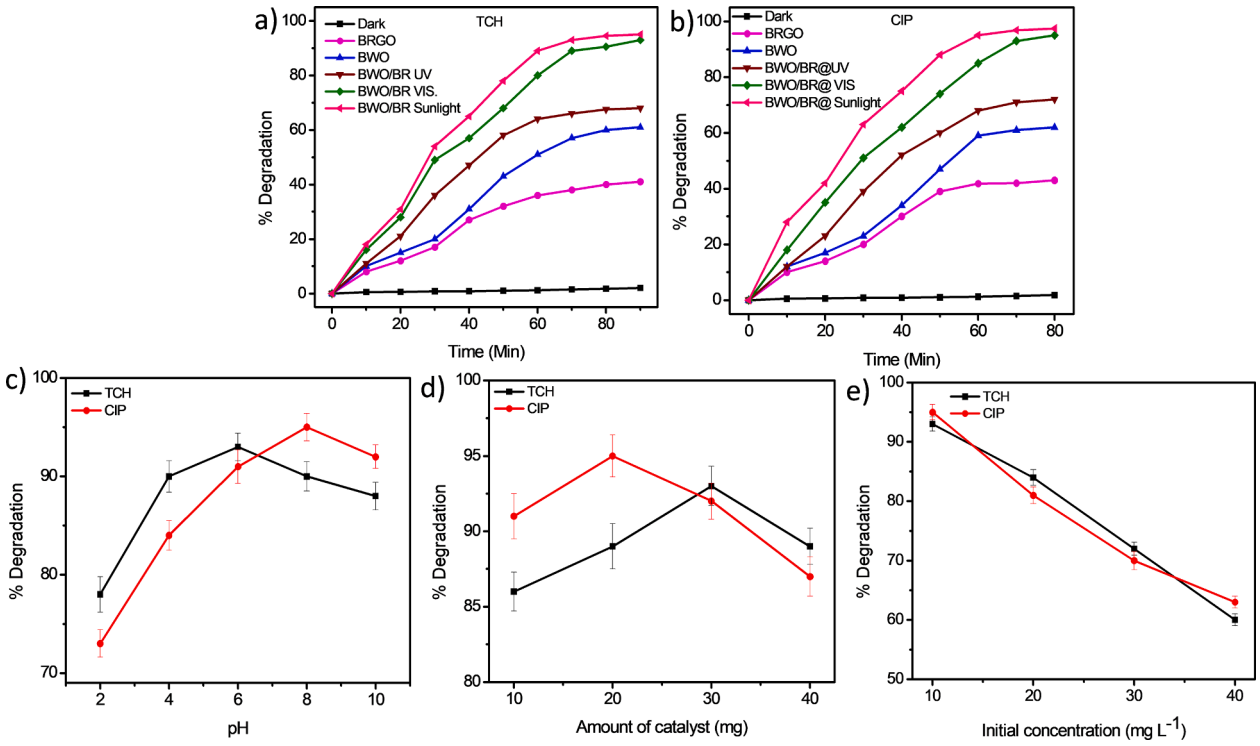

Fig. 8. (a) Degradation of TCH, (b) Degradation of CIP, (c) Effect of pH, (d) Effect of catalyst dosage and (e) Effect of initial concentration.

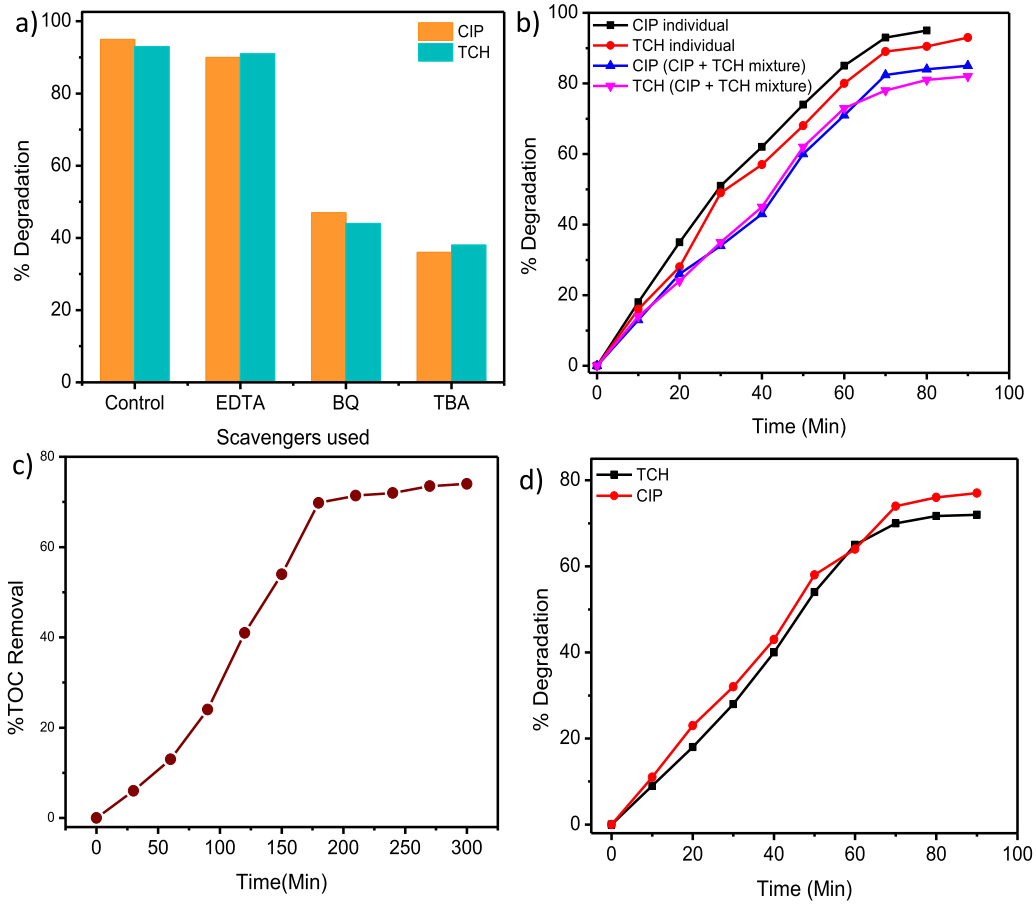

Fig. 9. (a) Scavenger studies, (b) Simultaneous degradation of TCH and CIP, (c) (a) % TOC Removal studies and (d) Degradation of TCH and CIP in real sample.

Table 1
Effect of photocatalytic degradation of TCH and CIP on inhibition zone of bacterial stains.

Irradiation time	*Inhibition zone diameter (mm)**			
	E. coli	L. *monocytogenes*	*S. typhimurium*	*S. aureus*
0	71	62	66	59
10	64	58	63	54
30	38	32	54	49
50	23	19	39	31
70	16	12	16	13
90	05	04	03	02

eV, respectively. Doped boron forms strong bonds with sp^2 and sp^3 carbon atoms, as seen by the peaks of BC3 (190.90 eV), BC2O (192.34 eV), and BCO2 (194.07 eV) in Fig. 6f [51]. The presence of the XPS 'B 1s' peak for BRGO proves that boron has been effectively doped into RGO. The surface area of the BWO and BWO/BR were examined for N_2 adsorption and desorption studies and displayed in Fig. S2. N_2 adsorption-desorption isotherm was found to be more BWO/BR (43.6 $m^2\ g^{-1}$) compared to BWO (29.6 $m^2\ g^{-1}$). The enhanced surface area of BWO/BR compared to BWO probably helps in enhancing the photocatalytic efficiency by reducing the recombination of photoexcited electrons and holes and swift mobility of electrons.

3.2. Optical properties

The light-harvesting abilities of BWO and BWO/BR were examined using UV-visible diffuse reflectance spectroscopy. Fig. 7a shows the sharp absorption edge of BWO at around 479 nm and emphasizes its ability to absorb visible radiation. An expected redshift is observed in the absorption of BWO upon addition of BRGO, and observed the absorption edge at around 520 nm. The corresponding Kubelka-Munk curves is given in Fig. 7b. It is found that the bandgaps of BWO and BWO/BR are found to be 2.73 and 2.22 eV, respectively. The incorporation of BRGO into BWO shows enhanced light absorption capacity, and the decreased bandgap suggests the probability of exhibiting enhanced photocatalytic behavior in the composite. The photoluminescence studies show the degree of effective photo-induced charge separation. Fig. 7c shows the strong peak at around 620 nm belonging to BWO due to recombination of phto-excited electrons and holes. A decrease in the intensity and broadening of the peak observed in BWO/BR could be attributed to quenching, the creation of metal defects due to BRGO, and a decreased bandgap. These results indicate the effective charge carrier separation occurring in BWO/BR. Efficient charge separation during photocatalysis was further studied using the electrochemical performances of the BWO and BWO/BR. The transient photocurrent response of BWO and BWO/BR is given in Fig. 7d. The current response studies were performed in the presence and absence of visible light in different cycles, consisting of 40 s per cycle. It is clear that both BWO and BWO/BR are capable of generating current in the presence of light. The efficiency of BWO/BR is two times higher than that of BWO, which indicates the occurrence of effective charge separation in BWO/BR. Electron Impedance Spectroscopy (EIS) studies were conducted to understand the effectiveness of charge separation. In Fig. 7e, the smaller arc observed in BWO/BR than BWO directs the lower charge transfer resistance. The addition of layered BRGO to BWO successfully reduces the transmission resistance of the surface electrons. The position of the conduction band in a semiconductor plays a crucial role in designing a promising photocatalyst. Mott-Schottkky (M-S) plots of BWO and BWO/BR are given in Fig. 7f. The conduction band edge potential (E_{CB}) of BWO and BWO/BR is found to be -0.72 and -1.03 V, respectively. The slopes indicate the n-type semiconductor characteristics. From the results of the bandgap of BWO and BWO/BR and the M-S plot, one can find out the edge potential of the valence band (E_{VB}).

3.3. Photocatalytic degradation studies

Two pharmaceutically important antibiotics (TCH and CIP) were selected as model pollutants for photocatalytic degradation studies. Photocatalytic degradation of TCH under different conditions is depicted in Fig. 8a. The profile indicates that the degradation of TCH can only take place under light but not in dark conditions. The degradation of TCH is found to be 41, 61 and 68 % respectively, in the presence of BRGO, BWO and BWO/BR, respectively, under UV radiation. The enhanced degradation (93 %) is observed in BWO/BR under visible light. Interestingly, the degradation of TCH is further increased in the presence of sunlight and was found to be 95 %. Almost the same trend is observed in the degradation of CIP. The degradation of CIP is high in the presence of BWO/BR and found to be 72, 95 and 97.5 %, respectively, under UV, visible light, and sunlight (Fig. 8b). In both cases, the degradation efficiency is highest in BWO/BR nanocomposite when compared to pristine materials. The enhanced activity in BWO/BR under sunlight indicates the capability of absorbing both UV and visible radiation. In addition, these degradation profile results are in good agreement with the optical and electrochemical characterizations.Even

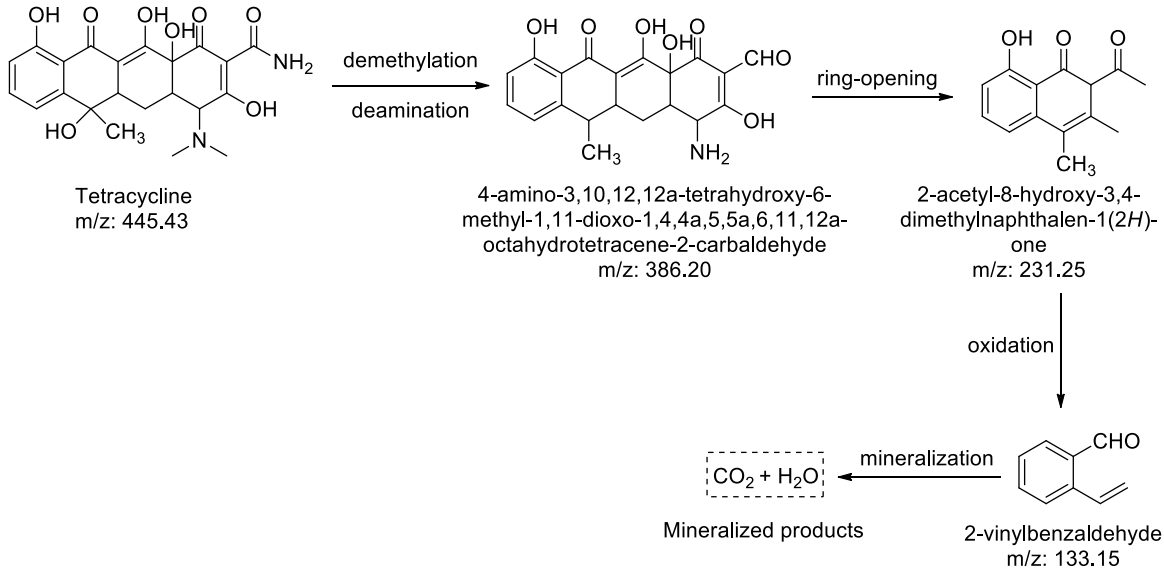

Scheme 3. Suggested photocatalytic degradation pathway of TCH.

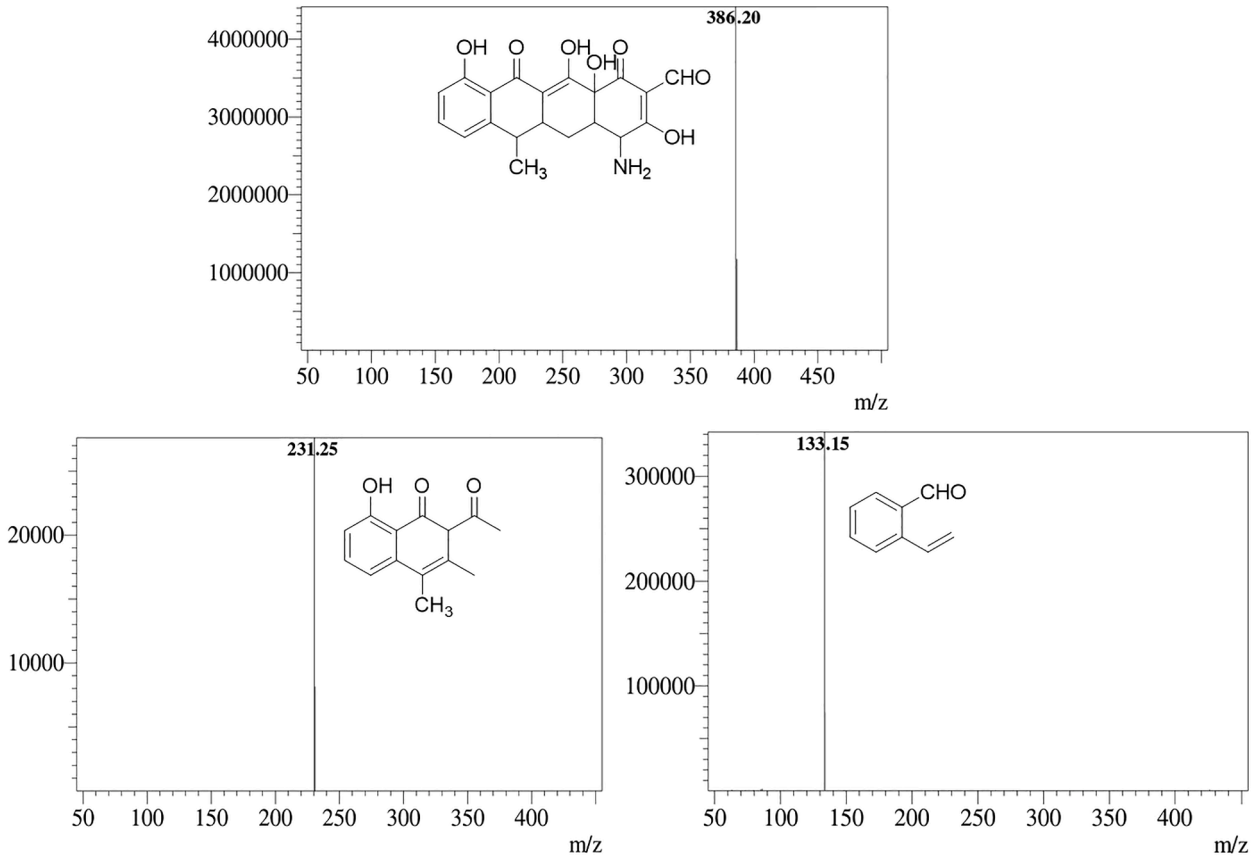

Fig. 10. Mass spectra of TCH intermediates.

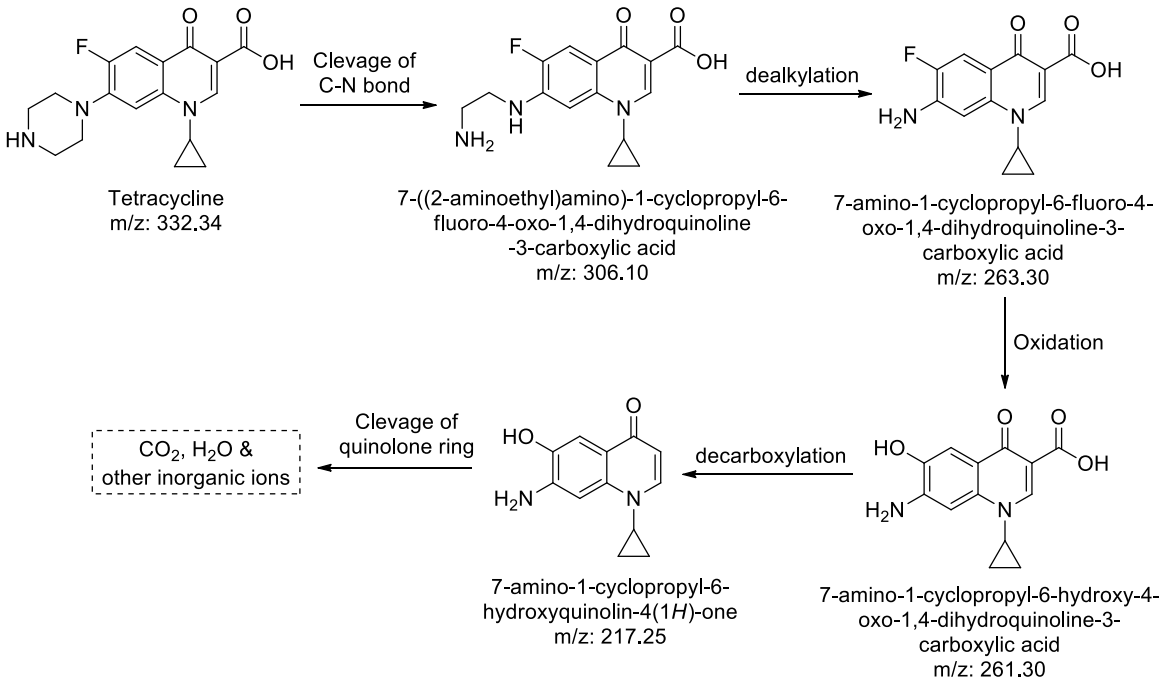

Scheme 4. Suggested photocatalytic degradation pathway of CIP.

though the degradation of TCH and CIP is high under sunlight, visible radiation was used for the optimization of reaction conditions. Since the flux and intensity keep changing every day, it is difficult to optimize under sunlight. In both cases, the degradation is low under acidic conditions (Fig. 8c). The maximum degradation of TCH is observed at pH 6. Upon further increase in the pH, the degradation was found to decline. The structure of the TCH may be destructed at too acidic and basic condition. Hence, a slightly acidic medium gives the maximum

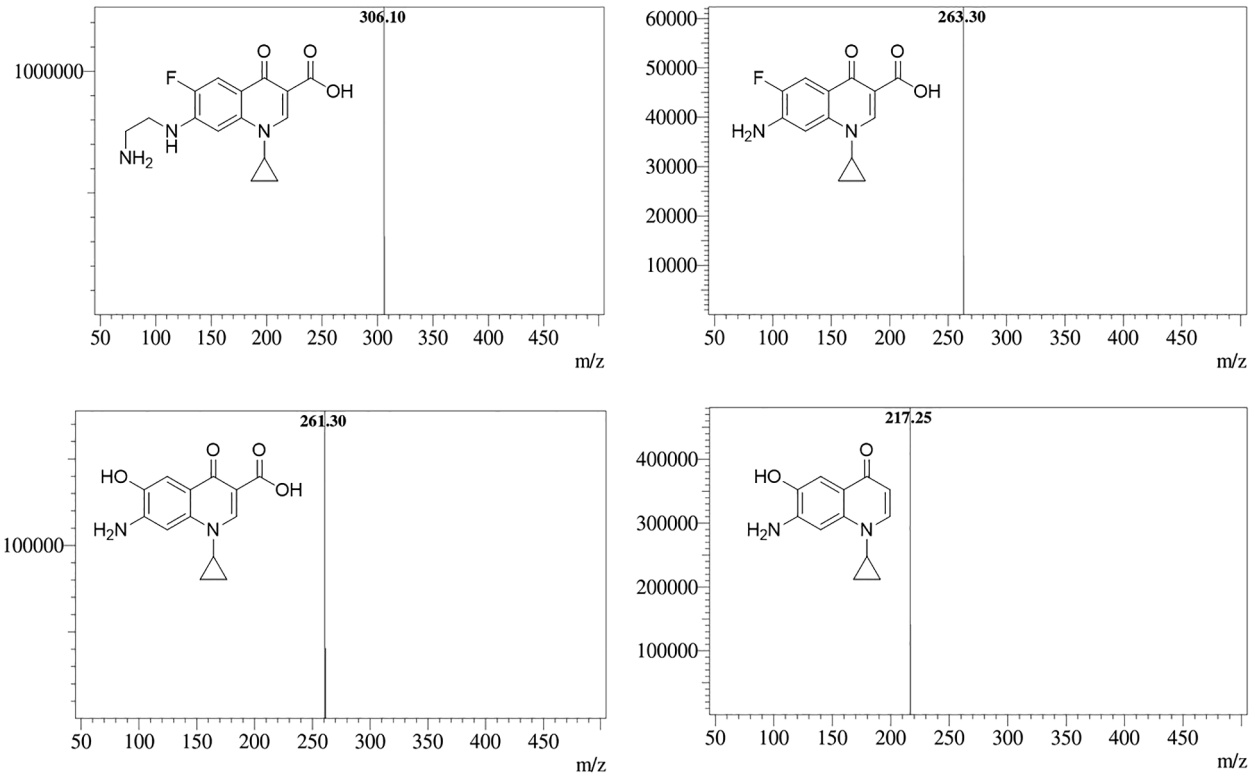

Fig. 11. Mass spectra of CIP intermediates.

efficiency. The TCH has proven to show three different equilibriums, like $TCH_3^+ \leftrightarrow TCH_2$, $TCH_2 \leftrightarrow TCH^-$, and $TCH^- \leftrightarrow TC_2^-$ equilibriums with the respective pKa of 3.3, 7.7 and 9.7, respectively. At lower acidic and basic pH, the efficiency found is lower due to the repulsion between the catalyst and TCH. The pH of the solution was varied from 2 to 10, and the degradation of CIP was examined. The maximum efficiency was found at pH 8. The pKa values of CIP are 6.09 and 8.7 belonging to carboxylic and nitrogen groups, respectively. The CIP was found to be more stable at an acidic pH, and its reported zwitterionic point is at pH 7.4. The degradation of CIP at an acidic pH is low due to the high concentration of H^+ ions that leads to the quenching of hydroxyl radicals. The basic pH aids in the formation of hydroxyl radicals, which in turn enhance the photocatalytic degradation of CIP. The amount of BWO/BR required for the degradation of TCH and CIP was evaluated under visible light. From Fig. 8d, it is found that 20 and 30 mg of BWO/BR are sufficient for the photocatalytic degradation of CIP and TCH, respectively. A decline in degradation efficiency is observed upon adding an increased amount of catalyst. This could be attributed to the increased concentration of suspended particles in solution, which results in weaker absorption and transmittance of light during the reaction. The effects of the initial concentrations of TCH and CIP in the presence of a catalyst were examined. The degradation efficiency decreased upon increasing the concentration of TCH and CIP. It found 93 and 95 % degradation of 10 mg L^{-1} of TCH and CIP (Fig. 8e). The degradation efficiency decreased to 60 and 63 %, respectively, for 40 mg L^{-1} of TCH and CIP. When the analyte concentration is higher, it eventually blocks the surface active sites of the catalyst, resulting in poor absorption of light.

3.4. Scavenger, simultaneous removal, TOC removal, real sample and residual antimicrobial activity studies

Reactive species responsible for the degradation of TCH and CIP were examined using scavenger studies. 5 mmol L^{-1} Ethylene diamine tetraacetic acid (EDTA), benzoquinone (BQ) and Tertiary butyl alcohol (TBA) are the scavengers used for holes, superoxide radicals, and hydroxyl ions, respectively. Fig. 9a indicates that the percentage of degradation is not affected when EDTA is used, but a considerable decline is observed in the presence of BQ and TBA. This shows that hydroxyl ions and superoxide radicals are the major reactive species generated during the phtoredox reaction between BWO/BR, TCH and CIP in the presence of light. The pharmaceutical effluent usually contains multiple stable organic molecules. Many pharmaceutical tablets are combinations of two or more active pharmaceutical ingredients. Hence, simultaneous degradation of TCH and CIP has been conducted to understand their efficiency. The TCH and CIP (1:1 ratio, 10 mg L^{-1} concentration) were examined individually under their respective λ_{max} and the degradation percentage is given in Fig. 9b. The TCH and CIP individual degradations in a mixture are found to be 82 and 85 %, respectively. The extent of mineralization of organic compounds is an important feature in photocatalytic degradation studies. Therefore, fusion UV/persulfate Total Organic Carbon (TOC) was examined. Fig. 9c shows the removal of 74 % of TOC in a span of 300 min. This shows the degradation of TCH and CIP into less hazardous byproducts and maximum removal of even intermediates formed during degradation. A pharmaceutical effluent sample (before treatment) was collected from the local pharmaceutical industry and examined for degradation of TCH and CIP. TCH and CIP (both 10 mg L^{-1} concentration) were added to filtered pharmaceutical effluent, and the degradation of TCH and CIP was examined under optimized conditions. Fig. 9d shows the obvious decrease in the degradation of TCH and CIP due to the presence of other inorganic ions and competing organic molecules. Still, the degradation of CIP and TCH was found to be 72 and 69 %, respectively.

The mineralization of the organic molecule is very essential for effective photocatalytic degradation. Sometimes, the toxicity of the intermediate itself is higher than the starting material. The photocatalytic degradation of TCH and CIP was subjected to residual antimicrobial analysis for four different antibacterial stains. The functional group present in TCH and CIP would be responsible for their antimicrobial activity. The zone of inhibition of all the stains (E. coli, L.

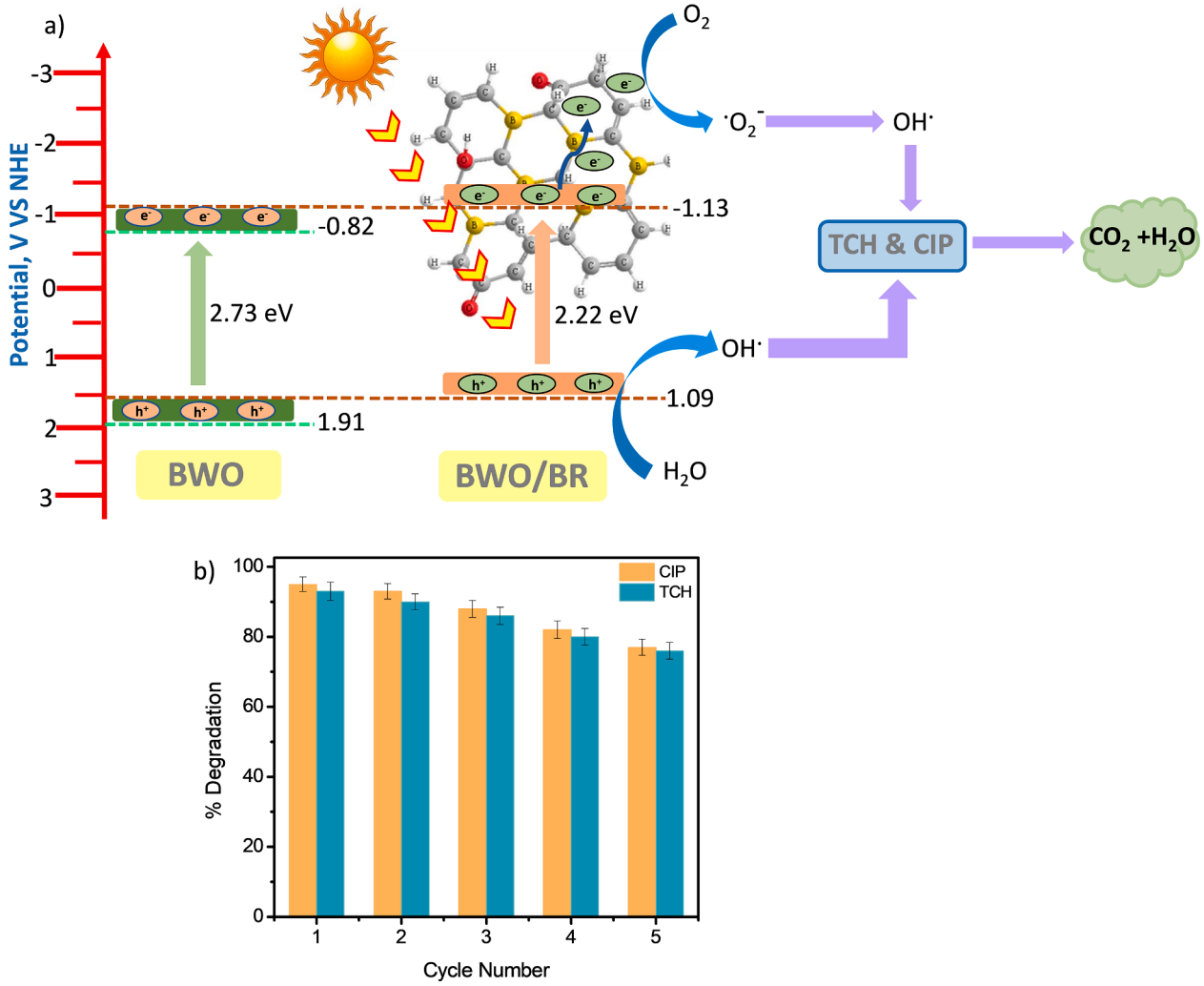

Fig. 12. (a) Mechanism of photocatalysis, (b) Reusability studies of BWO/BR.

monocytogenes, S. typhimurium, S. aureus) before irradiation with visible light and after irradiation for 90 min is given in Table 1. The TCH and CIP showed excellent antimicrobial activity against all stains in the presence of BWO/BR before irradiation. The zone of inhibition starts to decrease after ten minutes due to the decay of active functional groups present in TCH and CIP. An almost-zero zone of inhibition is observed at 90 min. This indicates the effective mineralization of TCH and CIP in the presence of BWO/BR and visible light.

3.5. Determination of degradation intermediates of TCH

The scheme of photocatalytic degradation of TCH in presence of BWO/BR is given in Scheme 3. LC-MS was employed to identify all the intermediates generated during photocatalytic degradation of TCH (Fig. 10). It has been observed that TCH is first transferred into ring product 4-amino-3,10,12,12a-tetrahydroxy-6-methyl-1,11-dioxo-1,4,4a,5,5a, 6,11,12a-octahydrotetracene-2-carbaldehyde with m/z value of 386.20 corresponding to the product of demethylation and deamination. Later, 2-acetyl-8-hydroxy-3,4-dimethylnaphthalen-1(2H)-one (m/z = 231.25) was formed due to the ring-opening reactions and the cleavage of carbon bond in compound 4-amino-3,10,12,12a-tetrahydroxy-6-methyl-1,11-dioxo-1,4,4a,5,5a, 6,11,12a-octahydrotetracene-2-carbaldehyde. The compound 2-acetyl-8-hydroxy-3,4-dimethylnaphthalen-1(2H)-one undergoes further oxidization, the compound 2-vinylbenzaldehyde with m/z value 133.15 was formed through carbon-bond cleavage. Finally, 2-vinylbenzaldehyde undergoes complete mineralization and degraded to form CO_2 and H_2O.

3.6. Determination of degradation intermediates of CIP

The possible degradation pathway of CIP is shown in Scheme 4. The intermediaries formed throughout the photocatalytic process were identified by LC-MS analysis (Fig. 11). Initially the degradation mechanism involves the attack of the piperazine ring by the oxidizing species produced on the photocatalyst surface. Given that piperazine owns a strong nucleophilic nature, photo-holes are attracted to the cyclic structure and break the C–N bonds, thus forming compound 7-((2-aminoethyl)amino)−1-cyclopropyl-6-fluoro-4-oxo-1,4-dihydroquinoline-3-carboxylic acid (m/z = 306.10). Then it undergoes dealkylation leads to the formation of 7-amino-1-cyclopropyl-6-fluoro-4-oxo-1,4-dihydroquinoline-3-carboxylic acid (m/z = 263.30). As the attack of OH radicals continue, the oxidation of the quinolone takes place with the incorporation of OH group in the aromatic ring results in the formation of compound 7-amino-1-cyclopropyl-6-hydroxy-4-oxo-1,4-dihydroquinoline-3-carboxylic acid (m/z = 261.30), which further undergoes decarboxylation results in formation of 7-amino-1-cyclopropyl-6-hydroxyquinolin-4(1H)-one (m/z = 217.25). Finally, destabilization of the quinolone group is eventually reached through the attack of the oxidative species, leading to the mineralization of the 7-amino-1-cyclopropyl-6-hydroxyquinolin-4(1H)-one and thus the generation of CO_2, H_2O and other molecules as mineralized products.

Table 2
Comparison of degradation of TCH and CIP reported materials.

Sl. No	Photocatalyst	Target Molecule	Light source	Degradation%, Time	Refs.
1	Au/b-TiO_2/rGO	TCH	Visible light	sonophotocatalytic ~100 % in 60 min	[52]
2	$CuBi_2O_4$/Bi_2WO_6	TCH	Visible light (300 W Xenon lamp)	93 % in 60 min	[53]
3	Cl doped g-C_3N_4	TCH	Visible light (300 W Xenon lamp)	92 %,120 min.	[54]
4	rGO/Cu_2O/Bi_2O_3	TCH	Visible light (250 W Xenon lamp)	75 %, 180 min.	[55]
5	Ag-α $NiMoO_4$	TCH	Visible light (150 W Xenon lamp)	80 %,180 min	[56]
6	Cu_2O/rGO/MoS_2 (Cu_2MG)	TCH	Visible light,	sonophotocatalytic ~100 %, 10 min	[57]
7	Bi_2WO_6/Ta_3N_5	CIP	Visible light,	81.1 %, 120 min	[58]
8	Fe_2O_3/Bi_2WO_6	CIP	Visible light,	65 %, H_2O_2 mediated, 120 min	[59]
9	Ag/silica	CIP	Visible light,	98.2 %, 180 min	[60]
10	ZnO/g-C_3N_4	CIP		93.8 %, 150 min	[61]
11	BiOCl/Cu-doped Bi_2S_3	CIP	UV-visible	97 %, 30 min	[62]
12	RGO/Bi_2WO_6	CIP	500 W xenon lamp	89.2 %, 180 min	[63]
13	PCN/BCN_x	CIP	300 W Xe lamp (λ > 420 nm	94.9 %, 120 min	[64]
14	BWO/BR	TCH	Solar light	95 %, 90 min	Present work
			Visible light	93 %, 90 min	
		CIP	Solar light	97.5 %,90 min	
			Visible light	95.0 %,90 min	

3.7. Mechanism of photocatalysis

The optical, electrochemical, scavenger studies, and intermediate determination results have been combined to elucidate the photocatalytic mechanism involved in the degradation of TCH and CIP (Fig. 12a). The electron spin resonance results (ESR) indicate the formation of hydroxyl and superoxide radicals during photocatalysis as observed in Fig. S3. Since both BWO and BWO/BR shows n-type semiconductor nature, the conduction band (CB) edge potential is considered +1 to the M-S plot obtained values. Upon irradiating light on Bi_2WO_6, excitation takes place effectively. This leads to the generation of photexcited electrons and holes. The electrons in the valence band (VB) of BWO leave behind holes and move to the CB. There is a probability of recombination of the electrons with the holes of the BWO valence band. When BWO is combined with BRGO, decrease in the rate of recombination of charge carriers is observed due to the decreased bandgap and enhanced conductivity. Upon combining BR to BWO, the edge potential of the BWO shows a slight deviation towards a more negative potential, which helps with the easy reduction of dissolved oxygen. The BR is known to have a π-conjugated system, a great surface area, and good conductivity, and withdraws the electrons from the CB of BWO and eventually separates the charge carriers. The BRGO helps for the mobility of electrons easily and makes them available for the reduction of dissolved oxygen. The dissolved oxygen then forms the superoxide radical and finally generates hydroxyl radicals as the major active species during photocatalysis. The holes in the VB of the BWO undergo oxidation and form hydroxyl radicals. The hydroxyl radicals generated from both sides degrade the TCH and CIP into carbon dioxide and water molecules. The stability of the catalyst is an important feature in photocatalytic degradation studies. Therefore, BWO/BR has been recovered and used for 5 cycles towards the degradation of TCH and CIP under optimum conditions. Fig. 12b depicts the regeneration plot and managed to exhibit the degradation efficiency of 76 and 77 % of TCH and CIP, respectively even at 5th cycle. XRD and SEM analysis for the used BWO/BR nanocomposite was conducted and the results are given in Fig. S4. A decrease in the crystallinity is observed after five cycles probably due to the photo corrosion and photo dissolution of BWO/BR. Furthermore, SEM analysis was used to examine the BWO/BR photocatalyst's morphology both before and after the photocatalytic reaction (Fig. S4b). The photocatalyst no longer has a porous structure and instead resembles clusters of particles that coalesce with one another after the fifth run. The photocatalytic efficiency of BWO/BR is good and comparable to many reported methods as shown in Table 2 [52–64].

4. Conclusions

Environmental remediation was done in the present work by targeting two major streams like use of spent lithium ion batteries as source of carbon and mineralization of hazardous antibiotics present in aqueous system. Graphite powder was obtained by waste Li-ion batteries and fabricated boron-doped RGO. The photocatalytic activity was found to increase in BWO upon anchoring with BRGO. The reduced bandgap, increased conductivity and surface area, formation of defects in the composite, and a decrease in electron and hole recombination are all possible explanations for the increased photocatalytic activity in BWO/BR. The simultaneous degradation of CIP and TCH speaks about the practical applicability of synthesized BWO/BR nanocomposite. ESR studies shows the generation of superoxide and hydroxyl radicals were the reactive active species during photocatalysis. Additionally, TOC removal, intermediate product analysis using LC-MS, and evaluation of TCH and CIP's antibacterial efficacy against four bacterial strains indicates the complete mineralization of TCH and CIP. Extraction of carbon from spent LIBs and producing heteroatom doped RGO could be used for generation of nanocomposite with any photoactive material. The carbon matrix that enhances the photocatalytic activity of semiconductors.

CRediT authorship contribution statement

K. Yogesh Kumar: Conceptualization, Data curation, Investigation, Writing – review & editing. **M.K. Prashanth:** Data curation, Formal analysis, Methodology, Writing – original draft. **H. Shanavaz:** Data curation, Formal analysis, Investigation. **L. Parashuram:** Formal analysis, Resources, Validation. **Fahd Alharethy:** Funding acquisition, Software, Supervision, Validation. **Byong-Hun Jeon:** Funding acquisition, Project administration, Writing – review & editing. **V.S. Anusuya Devi:** Formal analysis, Investigation. **M.S. Raghu:** Conceptualization, Investigation, Methodology, Resources, Supervision, Validation, Writing – review & editing.

Declaration of Competing Interest

The authors declare that they have no known competing financial interests or personal relationships that could have appeared to influence the work reported in this paper.

Data availability

Data will be made available on request.

Acknowledgment

The authors are immensely elated and wish to express their indebted gratitude to the Management of NHCE, BNMIT and Jain University for providing lab facilities to carry out this work. Authors extend their sincere appreciation to the Researchers Supporting Project Number (RSP2024R160), King Saud University, Riyadh, Saudi Arabia for the Support. This work was funded by the Korea Institute of Energy Technology Evaluation and Planning (KETEP) of the Republic of Korea (RS-2023-00255939).

Supplementary materials

Supplementary material associated with this article can be found, in the online version, at doi:10.1016/j.apsadv.2023.100569.

References

[1] K. Kummerer, Promoting resistance by the emission of antibiotics from hospitals and households into effluent, Clin. Microbiol. Infect. 9 (2003) 1203–1214.
[2] D. Li, R. Yuan, B. Zhou, H. Chen, Selective photocatalytic removal of sulfonamide antibiotics: the performance differences in molecularly imprinted TiO_2 synthesized using four template molecules, J. Clean. Prod. 383 (2023) 135470.
[3] U. Kumar, J. Kuntail, A. Kumar, R. Prakash, M.R. Pai, I. Sinha, *In-situ* H_2O_2 production for tetracycline degradation on Ag/s-(Co_3O_4/$NiFe_2O_4$) visible light magnetically recyclable photocatalyst, App. Surf. Sci. 589 (2022) 153013.
[4] K. Kummerer, Antibiotics in the aquatic environment – a review – part I, Chemosphere 75 (2009) 417–434.
[5] Y. He, Z. Huang, Z. Ma, B. Yao, H. Liu, L. Hu, Q. Zhao, Q. Yang, D. Liu, D. Du, Highly efficient photocatalytic performance and mechanism of α-ZnTcPc/g-C_3N_4 composites for methylene blue and tetracycline degradation under visible light irradiation, Appl. Surf. Sci. 498 (2019) 143834–143847.
[6] K. Yogesh Kumar, L. Parashuram, M.K. Prashanth, C.B. Pradeep Kumar, F. A. Alharti, P. Krishnaiah, J.B. Hun, M. Govindasamy, M.S. Raghu, N-doped reduced graphene oxide anchored with δ-Ta_2O_5 for energy and environmental remediation: efficient light-driven hydrogen evolution and simultaneous degradation of textile dyes, Adv. Powder Technol. 32 (2021) 2002–2012.
[7] A.A. Isari, Sono-photocatalytic degradation of tetracycline and pharmaceutical wastewater using WO_3/CNT heterojunction nanocomposite under US and visible light irradiations: a novel hybrid system, J. Hazard. Mater. 390 (2020) 122050–122064.
[8] L. Parashuram, M.K. Prashanth, P. Krishnaiah, C.B. Pradeep Kumar, F.A. Alharti, K. Yogesh Kumar, B.H. Jeon, M.S. Raghu, Nitrogen doped carbon spheres from Tamarindus indica shell decorated with vanadium pentoxide; photoelectrochemical water splitting, photochemical hydrogen evolution & degradation of Bisphenol A, Chemosphere 287 (2022) 132348–132362.
[9] I. Michael, L. Rizzo, C.S. McArdell, C.M. Manaia, C. Merlin, T. Schwartz, C. Dagot, D. Fatta-Kassinos, Urban wastewater treatment plants as hotspots for the release of antibiotics in the environment: a review, Water Res. 47 (2013) 957–995.
[10] S. Le, W. Li, Y. Wang, X. Jiang, X. Yang, X. Wang, Carbon dots sensitized 2 D–2 D heterojunction of $BiVO_4$/Bi_3TaO_7 for visible light photocatalytic removal towards the broad-spectrum antibiotics, J. Hazard. Mater. 376 (2019) 1–11.
[11] R. Mishra, S. Bera, R. Chatterjee, S. Banerjee, S. Bhattacharya, A. Biswas, S. Mallick, S. Roy, A review on Z/S – scheme heterojunction for photocatalytic applications based on metal halide perovskite materials, Appl. Surf. Sci. Adv. 9 (2022) 100241–100262.
[12] A. Alsulami, K. Yogesh Kumar, M.K. Prashanth, H. Shanavaz, L. Parashuram, C. B. Pradeep Kumar, B.H. Jeon, M.S. Raghu, Fabrication of $FeVO_4$/RGO nanocomposite: an amperometric probe for sensitive detection of methyl parathion in green beans and solar light-induced degradation, ACS Omega 49 (2022) 45239–45252.
[13] S. Das, T. Deka, P. Ningthoukhangjam, A. Chowdhury, R.G. Nair, A critical review on prospects and challenges of metal-oxide embedded g-C_3N_4-based direct Z-scheme photocatalysts for water splitting and environmental remediation, Appl. Surf. Sci. Adv. 11 (2022) 100273–100295.
[14] Y. Jiang, H. Zhang, Q. Chen, Z. Sun, L. Zeng, Constructing Z-scheme carbon-rich carbon nitride/TiO_2 photocatalyst for improved photocatalytic activity, Appl. Surf. Sci. Adv. 9 (2022) 100238–100246.
[15] K. Yogesh Kumar, M.K. Prashanth, L. Parashuram, B. Palanivel, B.H. Jeon, M. S. Raghu, Gadolinium sesquisulfide anchored N-doped reduced graphene oxide for sensitive detection and degradation of carbendazim, Chemosphere 296 (2022) 134030–134045.
[16] C. Thambiliyagodage, A. Kumara, M. Jayanetti, L. Usgodaarachchi, H. Liyanaarachchi, B. Lansakara, Fabrication of dual Z-scheme g-C_3N_4/Fe_2TiO_5/Fe_2O_3 ternary nanocomposite using natural ilmenite for efficient photocatalysis and photosterilization under visible light, Appl. Surf. Sci. Adv. 12 (2022) 100337–100349.
[17] P.I. Uma, U.S. Shenoy, D.K. Bhat, Doped $BaTiO_3$ cuboctahedral nanoparticles: role of copper in photocatalytic degradation of dyes, Appl. Surf. Sci. Adv. 15 (2023) 100408–100419.
[18] A.G. Alhamzani, T.A. Yousef, M.M. Abou Krisha, K. Yogesh Kumar, M.K. Prashanth, L. Parashuram, B.H. Jeon, M.S. Raghu, Fabrication of layered In_2S_3/WS_2 heterostructure for enhanced and efficient photocatalytic CO_2 reduction and various paraben degradation in water, Chemosphere 322 (2023) 138235–138247.
[19] X. Xiong, J. Zhang, C. Chen, S. Yang, J. Lin, J. Xi, Z. Kong, Novel 0D/2D Bi_2WO_6/MoSSe Z-schemeheterojunction for enhanced photocatalytic degradation and photoelectrochemical activity, Ceram. Int. 48 (2022) 31970–31983.
[20] C.J. Chang, J.K. Chen, K.S. Lin, Y.H. Wei, P.Y. Chao, C.Y. Huang, Enhanced visible-light-driven photocatalytic degradation by metal wire-mesh supported Ag/flower-like Bi_2WO_6 photocatalysts, J. Alloy. Compd. 813 (2020) 152186–152198.
[21] X. Zhang, Y. Zhang, H. Li, Y. Wang, M. Xiang, W. Yu, H. Huang, H. Ou, Surface cationic and anionic dual vacancies enhancing photocatalytic activity of Bi_2WO_6, Appl. Surf. Sci. 602 (2022) 154311–154320.
[22] T. Chen, L. Liu, C. Hu, H. Huang, Recent advances on Bi_2WO_6-based photocatalysts for environmental and energy applications, Chin. J. Catal. 42 (2021) 1413–1438.
[23] N.D. Phu, L.H. Hoang, P. Van Hai, T.Q. Huy, X.B. Chen, W.C. Chou, Photocatalytic activity enhancement of Bi_2WO_6 nanoparticles by Ag doping and Ag nanoparticles modification, J. Alloy. Compd. 824 (2020) 153914–153921.
[24] W. Liang, J. Pan, X. Duan, H. Tang, J. Xu, G. Tang, Biomass carbon modified flower-like Bi_2WO_6 hierarchical architecture with improved photocatalytic performance, Ceram. Int. 46 (2020) 3623–3630.
[25] H. Huang, C. Zhou, X. Jiao, H. Yuan, J. Zhao, C. He, J. Hofkens, M.B.J. Roeffaers, J. Long, J.A. Steele, Subsurface defect engineering in single-unit-cell Bi_2WO_6 monolayers boosts solar-driven photocatalytic performance, ACS Catal. 10 (2019) 1439–1443.
[26] J. Bai, X. Ren, X. Chen, P. Lu, M. Fu, Oxygen vacancy-enhanced ultrathin Bi_2O_3-Bi_2WO_6 nanosheets' photocatalytic performances under visible light irradiation, Langmuir 37 (2021) 5049–5058.
[27] X. Liu, S. Gu, Y. Zhao, G. Zhou, W. Li, $BiVO_4$, Bi_2WO_6 and Bi_2MoO_6 photocatalysis: a brief review, J. Mater. Sci. Technol. 56 (2020) 45–68.
[28] W.C. Huo, X.A. Dong, J.Y. Li, M. Liu, X.Y. Liu, Y.X. Zhang, F. Dong, Synthesis of Bi_2WO_6 with gradient oxygen vacancies for highly photocatalytic NO oxidation and mechanism study, Chem. Eng. J. 361 (2019) 129–138.
[29] S. Zhang, W. Pu, A. Chen, Y. Xu, Y. Wang, C. Yang, J. Gong, Oxygen vacancies enhanced photocatalytic activity towards VOCs oxidation over Pt deposited Bi_2WO_6 under visible light, J. Hazard. Mater. 384 (2020) 121478–121489.
[30] Y. Liu, B. Wei, L. Xu, H. Gao, M. Zhang, Generation of oxygen vacancy and OH radicals: a comparative study of Bi_2WO_6 and $Bi2WO_6$−x nanoplates, ChemCatChem 7 (2015) 4076–4084.
[31] J. Jin, J. Sun, K. Lv, X. Guo, Q. Hou, J. Liu, J. Wang, Y. Bai, X. Huang, Oxygen vacancy BiO_2-x/Bi_2WO_6 synchronous coupling with Bi metal for phenol removal via visible and near-infrared light irradiation, J. Colloid Interface Sci. 605 (2022) 342–353.
[32] G. Long, J. Ding, L. Xie, R. Sun, M. Chen, Y. Zhou, X. Huang, G. Han, Y. Li, W. Zhao, Fabrication of mediator-free g-C_3N_4/Bi_2WO_6 Z-scheme with enhanced photocatalytic reduction dechlorination performance of 2,4-DCP, Appl. Surf. Sci. 455 (2018) 1010–1018.
[33] H. Alrobei, M.K. Prashanth, C.R. Manjunatha, C.B. Pradeep Kumar, C. P. Chitrabanu, P.D. Shivaramu, K. Yogesh Kumar, M.S. Raghu, Adsorption of anionic dye on eco-friendly synthesised reduced graphene oxide anchored with lanthanum aluminate: isotherms, kinetics and statistical error analysis, Ceram. Int. Part B 47 (2021) 10322–10331.
[34] A.D. Vincenzo, D.C. Martino, E. Piacenza, P. Conte, A. Pettignano, G. Lazzara, P. L. Meo, Reduced graphene oxide/silver nanoparticles/β-cyclodextrin nanosponges composites with improved photocatalytic activity, Appl. Surf. Sci. Adv. 15 (2023) 100407–100416.
[35] A. Fattah-alhosseini, M. Molaei, M. Nouri, K. Babaei, Review of the role of graphene and its derivatives in enhancing the performance of plasma electrolytic oxidation coatings on titanium and its alloys, Appl. Surf. Sci. Adv. 6 (2021) 100140–101158.
[36] T.N. Vinuth Raj, P.A. Hoskeri, H.B. Muralidhara, B.P. Prasanna, K. Yogesh Kumar, F.A. Alharthi, M.S. Raghu, Tantalum pentoxide functionalized Nitrogen-doped reduced graphene oxide as a competent electrode material for enhanced specific capacitance in a hybrid supercapacitor device, J. Alloy. Compd. 861 (2021) 158572–158583.
[37] L. Feng, Z. Qin, Y. Huang, K. Peng, F. Wang, Y. Yan, Y. Chen, Boron, sulfur, and phosphorus-doped graphene for environmental applications, Sci. Total Environ. 698 (2019) 134239–134258.
[38] N.P.D. Ngidi, M.A. Ollengo, V.O. Nyamori, Tuning the properties of boron-doped reduced graphene oxide by altering the boron content, New J. Chem. 44 (2020) 16864–16876.
[39] A. Farhan, M. Zahid, N. Tahir, A. Mansha, M. Yaseen, G. Mustafa, M.A. Alamir, I. M. Alarif, I. Shahid, Investigation of borondoped graphene oxide anchored with copper sulphide flowers as visible light active photocatalyst for methylene blue degradation, Sci. Rep. 13 (2023) 9497–9515.
[40] H. Shanavaz, K. Yogesh Kumar, M.K. Prashanth, D. Radhika, L. Parashuram, F. A. Alharti, B.H. Jeon, M.S. Raghu, Boron doped RGO from discharged dry cells decorated Niobium pentoxide for enhanced visible light-induced hydrogen evolution and water decontamination, Surf. Interfaces 36 (2023) 102544–102557.

[41] K.S. Kim, Y. Zhao, H. Jang, S.Y. Lee, J.M. Kim, K.S. Kim, J.H. Ahn, P. Kim, J. Y. Choi, B.H. Hong, Large-scale pattern growth of graphene films for stretchable transparent electrodes, Nature 457 (2009) 706–710.
[42] L.Y. Jiao, X.R. Wang, G. Diankov, H.L. Wang, H.J. Dai, Facile synthesis of high-quality graphene nanoribbons, Nat. Nanotechnol. 5 (2010) 321–325.
[43] J.C.Y. Jung, P.C. Sui, J.J. Zhang, A review of recycling spent lithium-ion battery cathode materials using hydrometallurgical treatments, J. Energy Storage (2021) 102217–102238.
[44] C. Qinghao, H. Liwu, L. Jianbo, L. Yiteng, C. Yungui, A new approach to regenerate high-performance graphite from spent lithium-ion batteries, Carbon 189 (2022) 293–30415.
[45] K. He, Z.Y. Zhang, F.S. Zhang, Synthesis of graphene and recovery of lithium from lithiated graphite of spent Li-ion battery, Waste Manag. 124 (2021) 283–292.
[46] J.S. Ribeiro, M.B.J.G. Freitas, J.C.C. Freitas, Recycling of graphite and metals from spent Li-ion batteries aiming the production of graphene/CoO-based electrochemical sensors, J. Environ. Chem. Eng. 9 (2021) 104689–104698.
[47] S. Natarajan, K. Subramani, Y.S. Lee, M. Sathish, V. Aravindan, Sandwich layered $Li_{0.32}Al_{0.68}$ $MnO_2(OH)_2$ from spent Li-ion battery to build high-performance supercapacitor: waste to energy storage approach, J. Alloy. Compd., 827 (2020) 154336–154344.
[48] H. Aitahsaine, A.E. jaouhari, A. Slassi, M. Ezahri, A. Benlhachemi, B. Bakiz, F. Guinneton, J.R. Gavarri, Electronic band structure and visible-light photocatalytic activity of Bi2WO6: elucidating the effect of lutetium doping, RSC Adv. 6 (2016) 101105–101114.
[49] L. Liu, J. Liu, K. Sun, J. Wan, F. Fu, J. Fan, Novel phosphorus-doped Bi_2WO_6 monolayer with oxygen vacancies for superior photocatalytic water detoxication and nitrogen fixation performance, Chem. Eng. J. 411 (2021) 128629–128645.
[50] R. Preetha, M. Govinda raj, E. Vijayakumar, M.G. Narendran, E. Varathan, B. Neppolian, U. Jeyapaul, A.J. Bosco, Promoting photocatalytic interaction of boron doped reduced graphene oxide supported $BiFeO_3$ nanocomposite for visible-light-induced organic pollutant degradation, J. Alloy. Compd. 904 (2022) 164038–164052.
[51] Y. Yuan, B. Lai, P. Yang, Y. Zhou, Treatment of ammunition wastewater by the combined Fe0/air and Fenton process (1stFe0/Air-Fenton-2ndFe0/air), J. Taiwan Inst. Chem. Eng. 65 (2016) 286–294.
[52] V. Vinesh, A.R.M. Shaheer, B. Neppolian, Reduced graphene oxide (rGO) supported electron deficient B-doped TiO_2 (Au/B-TiO_2/rGO) nanocomposite: an efficient visible light sonophotocatalyst for the degradation of Tetracycline (TC), Ultrason. Sonochem. 50 (2019) 302–310.
[53] L. Wang, G. Yang, D. Wang, C. Lu, W. Guan, Y. Li, J. Deng, J. Crittenden, Fabrication of the flower-flake-like $CuBi_2O_4/Bi_2WO_6$ heterostructure as efficient visible-light driven photocatalysts: performance, kinetics and mechanism insight, Appl. Surf. Sci. 495 (2019) 143521.
[54] F. Guo, M. Li, H. Ren, X. Huang, K. Shu, W. Shi, C. Lu, Facile bottom-up preparation of Cl-doped porous g-C_3N_4 nanosheets for enhanced photocatalytic degradation of tetracycline under visible light, Sep. Purif. Technol. 228 (2019) 115770.
[55] H. Shen, J. Wang, J. Jiang, B. Luo, B. Mao, W. Shi, All-solid-state Z-scheme system of RGO-Cu_2O/Bi_2O_3 for tetracycline degradation under visible-light irradiation, Chem. Eng. J. 313 (2017) 508–517.
[56] S. Kumar Ray, D. Dhakal, G. Gyawali, B. Joshi, A. Raj Koirala, S. Wohn Lee, Transformation of tetracycline in water during degradation by visible light driven Ag nanoparticles decorated Λ-$NiMoO_4$ nanorods: mechanism and pathways, Chem. Eng. J. 373 (2019) 259–274.
[57] P.S. Selvamani, J.J. Vijaya, L.J. Kennedy, A. Mustafa, M. Bououdina, P.J. Sophia, R. J. Ramalingam, Synergic effect of Cu_2O/MoS_2/rGO for the sonophotocatalytic degradation of tetracycline and ciprofloxacin antibiotics, Ceram. Int. 47 (2021) 4226–4237.
[58] S. Li, J. Chen, S. Hu, H. Wang, W. Jiang, X. Chen, Facile construction of novel Bi_2WO_6/Ta_3N_5 Z-scheme heterojunction nanofibers for efficient degradation of harmful pharmaceutical pollutants, Chem. Eng. J. 402 (2020) 126165.
[59] S. Song, H. Chen, C. Li, D. Shi, Y. Ying, Y. Han, J. Xu, B. Hong, H. Jin, D. Jin, Magnetic Bi_2WO_6 nanocomposites: synthesis, magnetic response and their visiblelight-driven photocatalytic performance for ciprofloxacin, Chem. Phys. 530 (2020) 110614.
[60] M. Golmohammadi, H.H. Bojd, M. Shiva, Photocatalytic degradation of ciprofloxacin antibiotic in water by biosynthesized silica supported silver nanoparticles, Ceram. Int. 49 (2023) 7717–7726.
[61] D.V. Thuan, T.B.H. Nguyen, T. H.Pham, J. Kim, T.T.H. Chu, M.V. Nguyen, K. D. Nguyen, W.A. Al-onazi, M.O.S. Elshikh, Photodegradation of ciprofloxacin antibiotic in water by using ZnO-doped g-C_3N_4 photocatalyst, Chemosphere 308 (2) (2022) 136408. Part.
[62] F. Du, Z. Lai, H. Tang, H. Wang, C. Zhao, Construction and application of BiOCl/Cu-doped Bi_2S_3 composites for highly efficient photocatalytic degradation of ciprofloxacin, Chemosphere 287 (4) (2022) 132391. Part.
[63] Y. Li, L. Chen, Y. Wang, L. Zhu, Advanced nanostructured photocatalysts based on reduced graphene oxide-flower-like Bi_2WO_6 composites for an augmented simulated solar photoactivity activity, Mater. Sci. Eng. B 210 (2016) 29–36.
[64] M. Zhang, L. Tang, Y. Zhu, Y. Zhang, J. Liu, J. Wang, C. Feng, L. Qiao, Y. Chen, Conjugated polymers S-scheme homojunction with large internal electric field and matching interface for efficient visible light photocatalytic degradation of ciprofloxacin, J. Clean. Prod. 419 (2023) 138199.